Materials Today Physics 60 (2026) 101970

Contents lists available at ScienceDirect

Materials Today Physics

journal homepage: www.journals.elsevier.com/materials-today-physics

Disorder-tuned magnetism and magnetocaloric response in a layered $SrGd_2Al_2O_7$ single crystal

Ziyu W. Yang [a,b,1], Guoliang Gong [d,1], Feifei Yuan [e,f,1], Shuai Tang [b,c], Guangkai Zhang [b], Xubin Ye [b], Zhao Pan [b], Yu-Jia Zeng [a,*], Youwen Long [b,c,**]

[a] Key Laboratory of Optoelectronic Devices and Systems of Ministry of Education and Guangdong Province, College of Physics and Optoelectronic Engineering, Shenzhen University, Shenzhen, 518060, China
[b] Beijing National Laboratory for Condensed Matter Physics, Institute of Physics, Chinese Academy of Sciences, Beijing, 100190, China
[c] School of Physical Sciences, University of Chinese Academy of Sciences, Beijing, 100049, China
[d] College of Rare Earths, Jiangxi University of Science and Technology, Ganzhou, 341000, China
[e] Xiamen Tungsten Co., Ltd., Xiamen, 361004, China
[f] Rare Earth Advanced Materials Technology Innovation Center, Inner Mongolia Northern Rare Earth Advanced Materials Technology Innovation Co., Ltd., Baotou, 014030, China

ARTICLE INFO

Keywords:
Magnetocaloric effect
Cryogenic
Disorder
Gaussian-averaged Brillouin model
Entropy

ABSTRACT

We report the magnetic and magnetocaloric responses of $SrGd_2Al_2O_7$ single crystals, a Ruddlesden-Popper oxide that exhibits intrinsic A-site cation disorder. Structural analysis reveals significant Sr-Gd intermixing, which suppresses long-range magnetic order down to at least 2 K and preserves the full magnetic entropy reservoir of Gd^{3+}. To describe the magnetization behavior, we implement a Gaussian-averaged Brillouin (GAB) framework that accounts for the magnetic bond probability and exchange-strength variance arising from the crystallographic disorder. $SrGd_2Al_2O_7$ exhibits large magnetocaloric responses, achieving a maximum isothermal magnetic entropy change $\Delta S_{mag} = 42.6$ J kg^{-1} K^{-1} and adiabatic temperature change $T_{ad} = 22.0$ K at 7 T, surpassing the benchmark coolant $Gd_3Ga_5O_{12}$ under comparable conditions. The lattice entropy contribution is exceptionally low below 20 K, further establishing $SrGd_2Al_2O_7$ as a highly competitive cryogenic refrigerant and highlighting controlled structural disorder as a potent design strategy for high-performance magnetocaloric materials.

1. Introduction

The development of efficient and reliable cooling technologies at cryogenic regime (below 20 K) is critical for a wide range of applications, including space-borne detectors, quantum computing, and the liquefaction of helium and hydrogen [1,2]. Magnetic refrigeration, based on the magnetocaloric effect, has emerged as a promising solid-state alternative to conventional gas-compression methods, offering improved efficiency, compactness, and operational simplicity [3–5]. The performance of a magnetic refrigerator is fundamentally governed by the properties of its working agents, making the discovery and development of refrigerant solids a central scientific pursuit.

An ideal magnetocaloric material should possess high magnetic moment density, low lattice heat capacity, and magnetic ordering temperature well below the operational range to prevent the loss of cooling efficiency [6–8]. In this context, compounds containing Gd^{3+} ion are particularly attractive. With its large, isotropic spin-only moment ($S = 7/2$, $L = 0$) derived from half-filled 4*f* shell, Gd^{3+} ion offers a substantial magnetic entropy reservoir of $R\ln 8$ per ion and is largely unaffected by crystal-field effects [9–14]. For decades, gadolinium gallium garnet $Gd_3Ga_5O_{12}$ (GGG) has been the benchmark material in this field [15–18]. However, its performance remains far from the theoretical limit, thereby motivating ongoing efforts to discover superior alternatives.

A central challenge in designing high-performance magnetic refrigerants lies in the intrinsic trade-off between achieving high density of magnetic ions and the accompanying increase of exchange interactions, which tends to elevate the magnetic ordering temperature. An effective

* Corresponding author.
** Corresponding author.
E-mail addresses: yangziyu@pku.edu.cn (Z.W. Yang), yjzeng@szu.edu.cn (Y.-J. Zeng), ywlong@iphy.ac.cn (Y. Long).
[1] These authors contributed equally to this work.

https://doi.org/10.1016/j.mtphys.2025.101970
Received 6 November 2025; Received in revised form 20 November 2025; Accepted 2 December 2025
Available online 5 December 2025

strategy to overcome this limitation involves introducing mechanisms that suppress or frustrate the long-range magnetic order [19,20]. Geometric frustration, characteristic of lattices such as garnets and pyrochlores, is a well-established approach [21,22]. More recently, attention has shifted toward exploiting chemical or structural disorder, which can disrupt exchange pathways and stabilize disordered states that retain substantial entropy down to the lowest temperatures [23].

In this context, the Ruddlesden-Popper oxide $SrGd_2Al_2O_7$ offers a compelling platform. Its layered structure accommodates a high density of Gd^{3+} moments while the intrinsic A-site cation disorder (Sr-Gd intermixing) introduces a spatially random distribution of magnetic sites [24,25]. We analyze this system using a Gaussian-averaged Brillouin (GAB) model, a theoretical framework that goes beyond mean-field theory (MFT). This model quantitatively incorporates dual consequences of disorder: magnetic bond dilution and exchange-strength variance.

By applying the GAB model to our high-quality $SrGd_2Al_2O_7$ single crystals, we show that the magnetization behavior is quantitatively governed by this crystallographic disorder. The resulting magnetic frustration preserves the full magnetic entropy of the dense Gd^{3+} sublattice at low temperatures, leading to a strong magnetocaloric response. Our results establish structural disorder as a powerful, model-supported design parameter for engineering high-performance magnetocaloric materials.

2. Material and methods

2.1. Crystal growth

High-quality $SrGd_2Al_2O_7$ single crystal was grown using the Czochralski method. Stoichiometric amounts of $SrCO_3$ (AR grade, Sinopharm), Gd_2O_3 (4N, Changchun Institute of Applied Chemistry, CAS), and Al_2O_3 (AR grade, Sinopharm) were weighed as received, thoroughly mixed, pressed into pellets, and sintered at 1200 °C in air for 10 h. Then the powder samples were reground and pressed, heated at 1500 °C in air for another 10 h. The sintered discs were then transferred to a custom-built crystal-growth furnace equipped with medium-frequency induction heating, an iridium crucible (Φ-50 × 50 mm^3), and a high-purity N_2 atmosphere.

Crystal growth was performed at a pulling rate of 1 mm/h and a rotation speed of 10 rpm. To minimize internal thermal stresses and prevent cracking, the as-grown crystal was subjected to a slow-cooling annealing process (15–30 °C/h) before removal from the furnace. Finally, a crystal slice with dimensions of 8 × 4 × 1 mm^3 was cut and polished for subsequent characterization.

2.2. Characterization

The out-of-plane X-ray diffraction (XRD) patterns were collected using a Rigaku SmartLab 9 kW X-ray diffractometer. Back-reflection Laue patterns were obtained using a Photonic Sciences Laue camera. DC magnetization and susceptibility measurements were conducted in applied magnetic fields ranging from 0 to 7 T and temperatures between 2 and 300 K, using a Quantum Design PPMS-9 system (VSM insert). Heat capacity measurements were performed in the temperature range of 1.9–40 K under applied fields of 0, 1, 2, 3, 5, and 7 T using the same apparatus. To ensure optimal thermal contact, Apiezon N-grease was applied.

3. Theory and calculation

3.1. Long range dipolar interactions

The pairwise dipole-dipole interaction between magnetic moments μ_i and μ_j, separated by the position vector $\boldsymbol{r_{ij}}$, is described by:

$$\mathscr{H}_{\mathbf{DD}} = \frac{\mu_0}{4\pi}\sum_{i<j}\left[\frac{\mu_i\cdot\mu_j}{|\mathbf{r}_{ij}|^3} - \frac{3(\mu_i\cdot\mathbf{r}_{ij})(\mu_j\cdot\mathbf{r}_{ij})}{|\mathbf{r}_{ij}|^5}\right]. \quad (1)$$

In the mean-field theory (MFT) approximation, this long-range interaction is simplified into an internal dipolar molecular field $\mathbf{H_{DD}}$ that is linearly proportional to the bulk magnetization $\mathbf{M}$, as $\mathbf{H_{DD}} = \lambda_{DD}\mathbf{M}$. Here, λ_{DD} is the dipolar molecular-field coefficient, which is orientation-dependent for magnetization measured along a specific unit vector, with units of T/(μ_B/ion).

For the specific *I4/mmm* lattice, λ_{DD} is computed once and held fixed for each magnetic orientation. A real-space spherical cutoff is adopted: we sum over all Bravais lattice translations and basis Gd^{3+} sites within a radius R_{max} = 100 Å, and confirm convergence by cross-checks performed at 60 and 120 Å. For the given lattice constants, a = 3.7052 Å and c = 19.781 Å, this corresponds roughly to enumerating in-plane translations up to ±27–28 cells and along c up to ±5–6 cells (with spherical selection applied). Crucially, the macroscopic demagnetizing field is not included in λ_{DD}.

3.2. Gaussian-averaged Brillouin (GAB) model

The Gd^{3+} are treated as localized spins with total angular momentum quantum number $J = S = 7/2$ and Landé g-factor $g = 2$. The per-ion magnetization is denoted by $\mathbf{M}$ (with magnitude M), expressed in units of μ_B/ion. The external field H is expressed in tesla (T). In classical mean-field theory (MFT), the total effective field acting on a magnetic moment is the sum of the external field and the internal molecular field $\mathbf{H_{mol}} = \lambda\mathbf{M}$. The total molecular field coefficient λ is given by the sum of the exchange contribution (λ_{ex}) and the dipolar contribution (λ_{DD}) by $\lambda = \lambda_{ex} + \lambda_{DD}$ [6,11,13,23,26,27].

The mean-field self-consistency equation is used to determine the magnitude of the magnetization M, and it reads:

$$M = gJ\mu_B B_J(\beta\, gJ\, \mu_B[H + \lambda\, M]), \quad (2)$$

where $B_J(x)$ is the Brillouin function, and $\beta = (k_BT)^{-1}$. We adopt the Heisenberg convention where the exchange coupling $J_{ij} > 0$ for antiferromagnetic (AFM) coupling, so that the Hamiltonian reads:

$$\mathscr{H}_{ex} = \sum_{<ij>} J_{ij}\boldsymbol{S_i}\cdot\boldsymbol{S_j}. \quad (3)$$

Let z denotes the number of equivalent nearest neighbors, the mean-field exchange contribution then becomes:

$$\lambda_{ex} = -\frac{zk_B}{(g\mu_B)^2}\langle J_{ex}\rangle. \quad (4)$$

In systems with partial magnetic occupancy f, the exchange network is disrupted by site dilution and bond-to-bond fluctuations. We model this using a magnetic-bond probability $p = f^2$ (i.e., probability that a nearest-neighbor pair is connected by a Gd–Gd bond), along with a Gaussian distribution of exchange strengths on the existing bonds:

$$J_{ex} \sim \mathscr{N}\left(\langle J_{ex}\rangle, \sigma_J^2\right). \quad (5)$$

Summing over the z neighbors gives a mean exchange field $\lambda_{ex}M$, and a variance of the molecular-field coefficient σ_λ, reads:

$$\sigma_\lambda^2 = \frac{zk_B^2}{(g\mu_B)^4}\left[p\sigma_J^2 + p(1-p)\langle J_{ex}\rangle^2\right], \quad (6)$$

where σ_J^2 represents the bond-strength randomness.

We then compare the global goodness-of-fit against that of the pure-MFT baseline using the standard likelihood-based model selection criterion, the total Akaike Information Criterion (ΔAIC_{total}), to identify the optimal parameter pair in the (p, σ_J) plane. For a given pair (p, σ_J), we fit only the mean field value $\langle J_{ex}\rangle$ for each isotherm.

4. Results and discussion

4.1. Crystallographic analysis

Fig. 1 presents the Θ–2Θ X-ray diffraction scan collected from a single-crystal platelet with large, parallel faces. Only (00ℓ) reflections are observed across a wide 2Θ range, characterized by sharp, resolution-limited peaks and the absence of parasitic reflections. This pattern is consistent with a (001) surface orientation and confirms strict *c*-axis alignment of the crystal within the tetragonal structure. Back-reflection Laue diffraction, taken with the incident beam parallel to the *c*-axis, reveals a sharp, fourfold-symmetric spot pattern devoid of streaking or splitting, indicating low mosaicity and excellent crystallinity.

$SrGd_2Al_2O_7$ crystallizes in the tetragonal space group *I4/mmm* (No. 139), with lattice parameters $a = b = 3.7052$ Å and $c = 19.781$ Å ($Z = 2$). It adopts the $n = 2$ Ruddlesden-Popper structure, analogous to $Sr_3Ti_2O_7$, in which corner-sharing AlO_6 octahedra form double-layered perovskite slabs separated by rock-salt-type AO layers [24,25]. The A-site cation distribution is partially disordered: the Wyckoff 4*e* site (tricapped trigonal prism, O_9) is Gd-rich [0.86 Gd + 0.14 Sr], while the Wyckoff 2*b* site at (0, 0, 1/2) (cuboctahedral O_{12}) is Sr-rich [0.72 Sr + 0.28 Gd].

4.2. Magnetic susceptibility and magnetization

Fig. 2(a) presents the temperature-dependent effective moment, $\mu_{eff}(T)$, along with Curie-Weiss (CW) fits to the magnetic susceptibility. On warming, $\mu_{eff}(T)$ approaches the free-ion value expected for Gd^{3+}, while a pronounced low-temperature downturn indicates dominant antiferromagnetic (AFM) correlations. Linear CW fits to $\chi^{-1}(T)$ are nearly orientation-independent. For $H//c$, we obtain $\Theta_{CW}^{//c} = -4.9$ K (50–300 K) and −5.1 K (2–20 K), with corresponding effective moments of 7.91 and 7.92 μ_B per Gd^{3+}. For $H \perp c$, we find $\Theta_{CW}^{\perp c} = -5.1$ K (50–300 K) and −5.5 K (2–20 K), yielding effective moments of 7.99 and 8.01 μ_B per Gd^{3+}. This weak anisotropy is consistent with Heisenberg-like Gd^{3+}.

The magnetism arises from Gd^{3+} ions primarily occupying the Gd-rich 4*e* sublattice. When projected onto the *ab* plane, these sites form square nets within the perovskite slabs. Stacking along *c* is interrupted by the rock-salt AO layer, suppressing interlayer coupling and favoring dominant in-plane interactions. The A-site intermixing introduces two critical effects: (i) effective dilution of the magnetic network in the Gd-rich layers, quantified by a bond probability *p* and (ii) a distribution of exchange strengths arising from local distortions in Gd–O–Gd bond geometries.

We therefore employ the Gaussian-averaged Brillouin (GAB) model, incorporating the magnetic bond probability *p* and the exchange-width σ_J. Both parameters are held constant within each field orientation. To

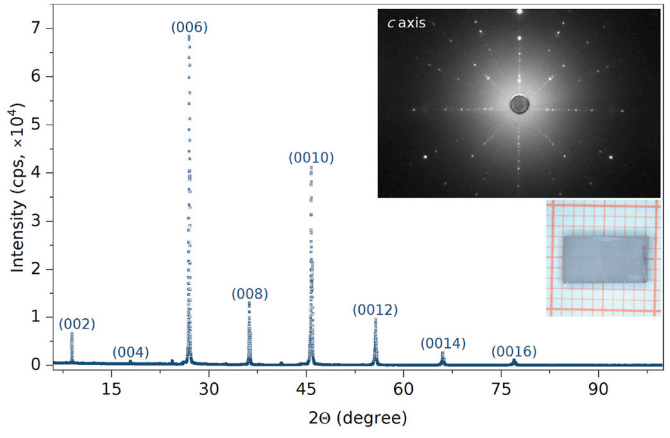

Fig. 1. Out-of-plane (Θ-2Θ) XRD of a $SrGd_2Al_2O_7$ single crystal (Cu $K\alpha$). Only the (00ℓ) reflections are observed, consistent with a (001) surface and *c*-axis alignment in the tetragonal *I*4/mmm structure. Inset: Photograph of the platelet single crystal used in this study, the broad faces correspond to the (001) plane; back-reflection Laue pattern with the incident beam // *c*, showing fourfold symmetry and sharp spots, further confirming *c*-axis orientation and good crystallinity.

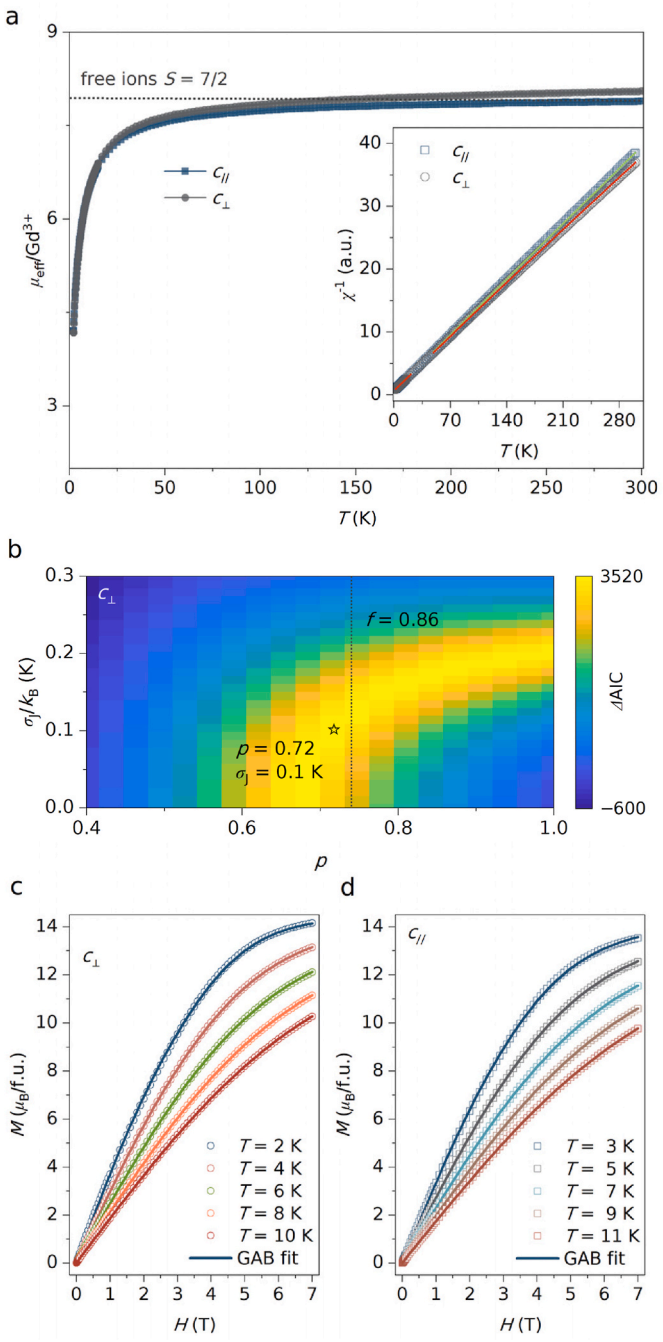

Fig. 2. Magnetic susceptibility and GAB modeling of magnetization data. (a) Temperature dependence of the effective moment, μ_{eff} (*T*), for fields $H \perp c$ and $H // c$. The dashed line marks the free-ion limit for Gd^{3+} ions ($S = 7/2$). The low-*T* downturn evidences predominant antiferromagnetic correlations. Inset: Curie-Weiss fits to χ^{-1} (*T*) over temperature ranges 2–20 K and 50–300 K; Θ_{CW} is more negative for $H \perp c$. (b) ΔAIC map from the GAB analysis scanning the probability *p* and the exchange-width σ_J/k_B. The optimum occurs near $p = 0.72$ and $\sigma_J \approx 0.10$ K (star), close to the crystallographic Sr-Gd mixing fraction ($f \approx 0.86$, Wyckoff 4*e*). (c–d) Isothermal *M*(*H*, *T*) curves (symbols) and global GAB fits (solid lines) up to 7 T: $H \perp c$ at $T = 2$, 4, 6, 8 and 10 K (c) and $H // c$ at $T = 3$, 5, 7, 9 and 11 K (d).

account for the long-range dipolar background, we compute orientation-dependent molecular-field offsets: $\lambda_{DD}^{//c} = -0.0627$ and $\lambda_{DD}^{\perp c} = +0.0314$ T/(μ_B/ion). The fixed dipolar offsets $\lambda_{DD}^{//c}$ and $\lambda_{DD}^{\perp c}$ are used as input, ensuring that the fitted exchange reflects true short-range interactions.

In both geometries, the GAB model provides a significantly better fit than pure MFT, as shown in Fig. 2(b) and Supplementary Fig. S1 and S2. Notably, the crystallographic expectations with a random Gd occupancy of 0.86 on the 4e site (probability 0.86 × 0.86 = 0.74), is in excellent agreement with the fitted $p_\perp = 0.72$, and marginally larger than $p_{//} = 0.65$, where the dipolar counter-term is stronger. The final global fit reproduces the measured $M(H)$ curves quite well, yielding small AFM average exchanges: $J_{ex}^{//c} = 0.334$ K and $J_{ex}^{\perp c} = 0.399$ K. The modest 20 % anisotropy in J_{ex} between orientations is fully consistent with an underlying isotropic microscopic exchange on Gd^{3+}, which arises primarily from the dipolar offsets of opposite sign and from bond dilution.

4.3. Heat capacity and entropy

Fig. 3(a) shows the nil-field heat capacity C_p of a (001)-oriented $SrGd_2Al_2O_7$ single crystal measured from 2 to 40 K. The lattice contribution is modeled by a combined Debye–Einstein fit, yielding a Debye temperature $\Theta_D = 257$ K and an Einstein temperature $\Theta_E = 131$ K. Subtracting this phonon baseline yields the magnetic heat capacity, defined as $C_{mag}(T, H) = C_p(T, H) - (C_D + C_E)$, as shown in Fig. 3(b). No λ-type anomaly is observed down to 2 K in any field, whereas broad humps emerge at 5 T and 7 T, consistent with Zeeman-split multiplet excitations of the Gd^{3+} ions.

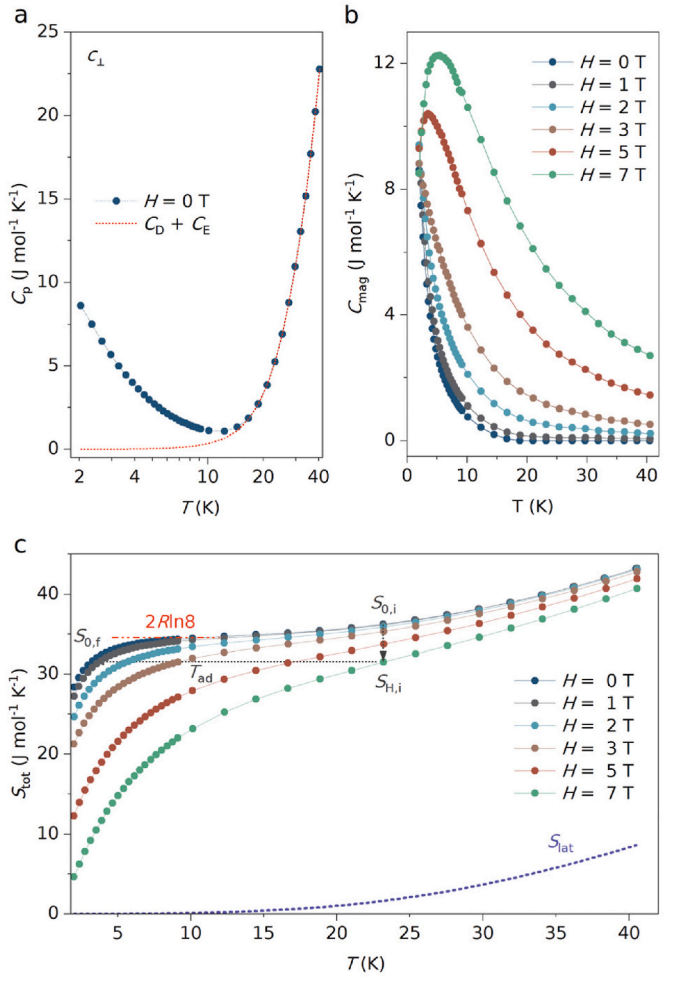

Fig. 3. Heat capacity and entropy along $H \perp c$. (a) Nil-field $C_p(T)$ of a (001)-oriented $SrGd_2Al_2O_7$ single crystal; the dotted curve is the lattice baseline $C_D + C_E$ from a Debye-Einstein fit. (b) Magnetic heat capacity $C_{mag}(T, H) = C_p - (C_D + C_E)$ for H = 0, 1, 2, 3, 5 and 7 T, respectively. (c) Total entropy $S_{tot}(T, H)$ obtained by integrating C_p/T, and the lattice contribution S_{lat} (dotted line), see text for detail. The vertical drop $S_{0,\,i} \rightarrow S_{H,\,i}$ illustrates the magnetic entropy change ΔS_{mag} $(T, H) = S_{0,\,i} - S_{H\,i}$; the horizon arrow $S_{H,\,i} \rightarrow S_{0,\,f}$ defines the adiabatic temperature change T_{ad} at constant entropy. The red dashed line marks the free-ion limit 2Rln8 for two Gd^{3+} ions.

Fig. 3(c) presents the total entropy, $S_{tot}(T, H) = S_{lat} + S_{mag}$, where S_{lat} represents the lattice entropy and S_{mag} is the magnetic entropy, calculated by integrating C_{mag}/T up to $T_{max} = 40$ K. For $H = 0$ and 1 T, we assume that the full magnetic entropy is recovered by 40 K, which is justified since $C_{mag} \rightarrow 0$ as $T \rightarrow 40$ K. For higher fields, a T^2 extrapolation is employed. The entropy is numerically calculated as:

$$S_{mag}(T,H) = S_{full} - \int_T^{T_{max}} \frac{C_{mag}(\tau,H)}{\tau} d\tau, \tau \in [T_{min}, T_{max}] \quad (7)$$

where S_{full} is the theoretical saturation entropy of Gd^{3+}, and T_{min}, T_{max} corresponds to the temperature limit reached in the measurement.

The resulting nil-field entropy becomes temperature-independent above $T = 7.5$ K, consistent with the full release of magnetic entropy from a degenerate ground-state multiplet of spin $S = 7/2$. The lattice entropy S_{lat} remains small compared to the total entropy S_{tot} at $T = 20$ K. A typical ratio of $S_{lat}/S_{mag} = 0.03$ is obtained, substantially lower than that of $GdPO_4$ (0.42), enabling more simplified Carnot cooling cycles below 20 K [28].

4.4. Magnetocaloric effect and efficiency

We evaluate the magnetocaloric effect for the $H \perp c$ configuration using two fully independent methods to determine the magnetic entropy change ΔS_{mag}: (i) the Maxwell relation applied to the isothermal $M(H, T)$ dataset, and (ii) direct calorimetry via numerical integration of C_p/T. As shown in Fig. 4(a), the results from both approaches converge onto a single curve within experimental uncertainty (open vs filled symbols), thereby validating our data consolidation process. Quantitatively, ΔS_{mag} reaches 42.6 J kg^{-1} K^{-1} at 7 T, surpassing the canonical garnet $Gd_3Ga_5O_{12}$, which yields 42.4 J kg^{-1} K^{-1} only at 9 T [6,16,29,30]. Adiabatic temperature changes, T_{ad}, are extracted from isentropic contours of the total entropy $S_{tot}(T, H)$, as illustrated schematically in Fig. 3(c) and summarized in Fig. 4(b). The maximum adiabatic temperature change attains 22.0 K at 7 T.

We further evaluate the intrinsic caloric efficiencies that quantify the useable heat $|Q|$ transferred per unit of actuator work $|W|$. The absorbed heat is computed by integrating $\mu_0 T_0 (\partial M/\partial T)_H$, while the mechanical and electrical input energies correspond to permanent-magnet and solenoidal actuation, respectively [31–33]. We report two dimensionless efficiency metrics across the 1–7 T field range and 2–14 K temperature window: a mechanical efficiency η_{mec} spanning 17–69 %, and an electrical efficiency η_{elec} ranging from 1.1 to 2.9 %, as plotted in Fig. 4(c). These values are competitive with those of other oxide-based refrigerants under comparable conditions [31,32].

The combination of large ΔS_{mag} and sizable T_{ad} at moderate fields can be attributed to two key structural features: the layered Ruddlesden-Popper topology of the Gd^{3+} sublattice, and the A-site Sr/Gd disorder. These jointly delay magnetic ordering and maintain a broad, field-tunable entropy reservoir across the 2–12 K window.

4.5. Scaling analysis

The relative cooling power is defined as $RCP(H) = \Delta S_{pk}(H)\, \delta T_{FWHM}(H)$, where ΔS_{pk} is the peak magnetic entropy change and δT_{FWHM} is the full width at half maximum of the ΔS_{mag} curve. The field dependence of RCP is well described by a power-law scaling $RCP(H) = AH^{1+1/\delta}$, yielding a critical exponent $\delta = 1.5$, i.e., RCP $\propto H^{1.7}$ [34]. This relation

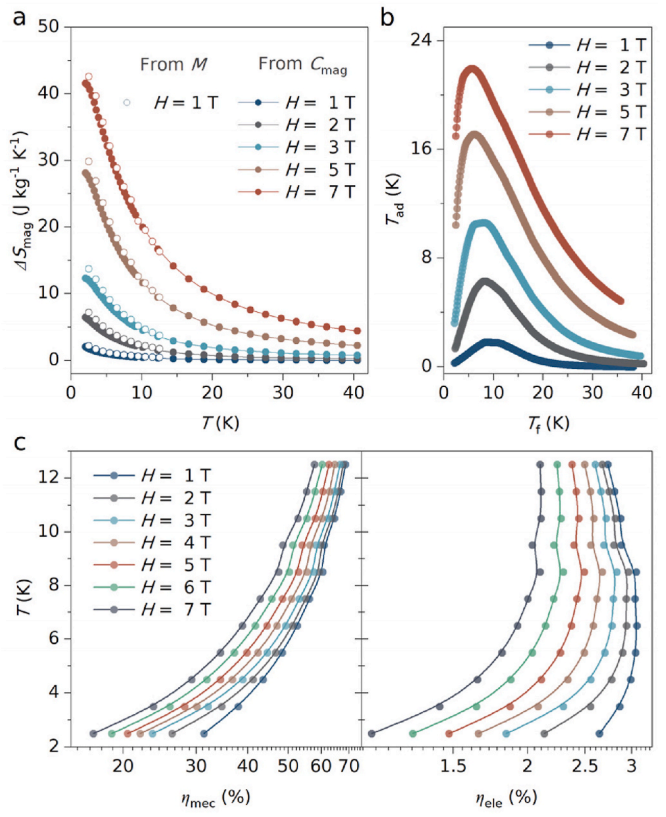

Fig. 4. (a) Isothermal magnetic entropy change ΔS_{mag} (T, H) for H = 0, 1, 2, 3, 5 and 7 T. Open symbols: Maxwell relation from $M(H, T)$; filled symbols: integration of C_p/T. The two routes coincide within uncertainty, confirming the data consolidation process. (b) Adiabatic temperature change T_{ad} as a function of final temperature T_f, obtained from isentropic constructions of $S_{tot}(T, H)$. (c) The mechanical and electrical efficiency under varied fields (1–7 T) and operating temperature (2–14 K).

quantitatively captures the rapid increase in cooling capacity with field in $SrGd_2Al_2O_7$ and reflects the near mean-field behavior of the system.

Following the Franco procedure for second-order magnetocaloric materials, we normalize the $\Delta S_{mag}(T, H)$ and rescale the temperature axis using a reduced variable T_{red}, taken as the temperature at which ΔS_{mag} reaches half its maximum value [1,34]. Under this normalization, all 64 $\Delta S_{mag}(T, H)$ curves collapse onto a single universal master curve, as shown in Fig. 5(b).

To further quantify the field response of the magnetocaloric effect, we extract the field exponent $n(T)$, which describes the sensitivity of $\Delta S_{mag}(T, H)$ to applied field, as [35,36]:

$$n(T,H) = \frac{\partial \ln |\Delta S_{mag}(T,H)|}{\partial \ln H}. \quad (8)$$

The maximum value of $n(T)$ approaches 2 in the high-temperature paramagnetic regime, consistent with Curie-law behavior, $\Delta S_{mag} \propto H^2/T^2$. This trend aligns with both the observed universal-curve collapse and the RCP scaling ($\delta = 1.5$).

5. Conclusions

To conclude, we demonstrate that single crystals of $SrGd_2Al_2O_7$, which exhibit significant A-site cation intermixing, possess magnetic properties governed primarily by this intrinsic structural disorder. As standard mean-field theory failed to capture the observed behavior, we introduced a Gaussian-averaged Brillouin model that explicitly incorporates magnetic bond probability p and exchange-strength variance σ_J. This model accurately reproduces the magnetization curves and

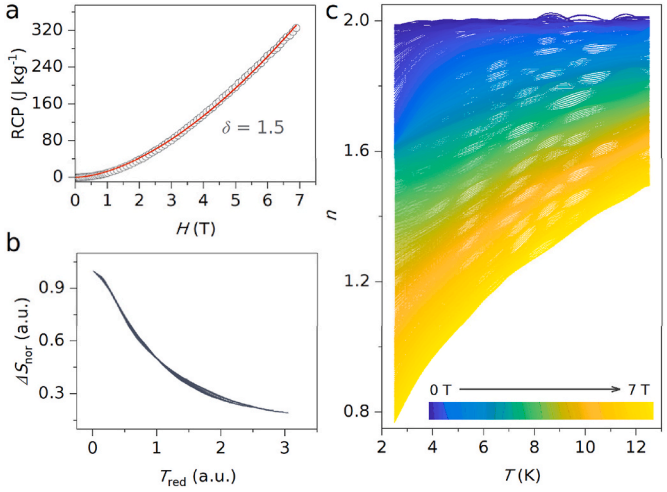

Fig. 5. (a) Relative cooling power, RCP as a function of field up to H = 7 T; red solid line is the power-law fit using RCP $\propto H^{1+1/\delta}$. (b) Universal master curve: 64 traces of ΔS_{nor} *vs* reduced temperature T_{red} collapse onto a single curve. (c) Temperature dependence of the field exponent $n(T)$ extracted from $\Delta S_{mag}(T, H)$ for 0–7 T (color scale), with $n \to 2$ approaching the paramagnetic limit.

yields fitted parameters that quantitatively match the crystallographic disorder. These results confirm that such disorder effectively suppresses long-range antiferromagnetic ordering down to 2 K, thereby preserving the full magnetic entropy for field-driven manipulation in the cryogenic regime.

As a result, $SrGd_2Al_2O_7$ exhibits a large magnetocaloric effect, achieving a maximum ΔS_{mag} of 42.6 J kg^{-1} K^{-1} and an adiabatic temperature change T_{ad} of 22.0 K at 7 T, surpassing the benchmark garnet refrigerant $Gd_3Ga_5O_{12}$. The material also benefits from an exceptionally low lattice entropy contribution (S_{lat}/S_{mag} = 0.03 at T = 20 K), enabling efficient and simplified cooling cycles. Our findings identify $SrGd_2Al_2O_7$ as a promising cryogenic refrigerant and establish that engineering A-site disorder in layered Ruddlesden-Popper structures is a powerful strategy for optimizing magnetocaloric performance.

CRediT authorship contribution statement

Ziyu W. Yang: Conceptualization, Investigation, Formal analysis, Writing - Original Draft, Funding acquisition. **Guoliang Gong:** Investigation. **Feifei Yuan:** Investigation. **Shuai Tang:** Investigation. **Guangkai Zhang:** Investigation. **Xubin Ye:** Investigation. **Zhao Pan:** Investigation. **Yu-Jia Zeng:** Supervision, Funding acquisition. **Youwen Long:** Supervision, Funding acquisition.

Declaration of competing interest

The authors declare that they have no known competing financial interests or personal relationships that could have appeared to influence the work reported in this paper.

Acknowledgements

This work was supported by the National Key R&D Program of China [grant number 2021YFA1400300]; the Guangdong Basic and Applied Basic Research Foundation [grant number 2022A1515111009]; the National Natural Science Foundation of China [grant numbers 12425403, 12261131499, 52273298].

Appendix A. Supplementary data

Supplementary data to this article can be found online at https://doi.

org/10.1016/j.mtphys.2025.101970.

Data availability

Data will be made available on request.

References

[1] V. Franco, J.S. Blázquez, J.J. Ipus, J.Y. Law, L.M. Moreno-Ramírez, A. Conde, Magnetocaloric effect: from materials research to refrigeration devices, Prog. Mater. Sci. 93 (2018) 112–232, https://doi.org/10.1016/j.pmatsci.2017.10.005.

[2] C. Hagmann, D.J. Benford, P.L. Richards, Paramagnetic salt pill design for magnetic refrigerators used in space applications, Cryogenics 34 (1994) 213–219, https://doi.org/10.1016/0011-2275(94)90171-6.

[3] A. Kitanovski, Energy applications of magnetocaloric materials, Adv. Energy Mater. 10 (2020): 1903741, https://doi.org/10.1002/aenm.201903741.

[4] J. Lyubina, Magnetocaloric materials for energy efficient cooling, J. Phys. D Appl. Phys. 50 (2017): 053002, https://doi.org/10.1088/1361-6463/50/5/053002.

[5] N.A. de Oliveira, P.J. von Ranke, Theoretical aspects of the magnetocaloric effect, Phys. Rep. 489 (2010) 89–159, https://doi.org/10.1016/j.physrep.2009.12.006.

[6] J.A. Barclay, W.A. Steyert, Materials for magnetic refrigeration between 2 K and 20 K, Cryogenics 22 (1982) 73–80, https://doi.org/10.1016/0011-2275(82)90098-4.

[7] W.E. Gifford, Refrigeration to Below 20 K, 10, Cryogenics, 1970, pp. 23–27, https://doi.org/10.1016/s0011-2275(70)80005-4.

[8] P.J. Shirron, Applications of the magnetocaloric effect in single-stage, multi-stage and continuous adiabatic demagnetization refrigerators, Cryogenics 62 (2014) 130–139, https://doi.org/10.1016/j.cryogenics.2014.03.014.

[9] P. Telang, T. Treu, M. Klinger, A.A. Tsirlin, P. Gegenwart, A. Jesche, Adiabatic demagnetization refrigeration with antiferromagnetically ordered $NaGdP_2O_7$, Phys. Rev. B 111 (2025): 064431, https://doi.org/10.1103/PhysRevB.111.064431.

[10] A. Jesche, N. Winterhalter-Stocker, F. Hirschberger, A. Bellon, S. Bachus, Y. Tokiwa, A.A. Tsirlin, P. Gegenwart, Adiabatic demagnetization cooling well below the magnetic ordering temperature in the triangular antiferromagnet $KBaGd(BO_3)_2$, Phys. Rev. B 107 (2023): 104402, https://doi.org/10.1103/PhysRevB.107.104402.

[11] Z.W. Yang, S. Qin, J. Zhang, D. Lu, H. Zhao, C. Kang, H. Cui, Y. Long, Y.-J. Zeng, Gadolinium oxyorthogermanate Gd_2GeO_5: an efficient solid refrigerant material for magnetic cryocoolers, Mater. Today Phys. 27 (2022): 100810, https://doi.org/10.1016/j.mtphys.2022.100810.

[12] Z. Yang, S. Qin, X. Ye, Z. Liu, Y. Guo, H. Cui, J.-y. Y. Ge, H. Li, Y. Long, Y.J. Zeng, Large magnetic entropy change in weberite-type oxides Gd_3MO_7 (M = Nb, Sb, and Ta), Sci. China Phys. Mech. Astron. 65 (2022): 247011, https://doi.org/10.1007/s11433-021-1834-4.

[13] E.C. Koskelo, C. Liu, P. Mukherjee, N.D. Kelly, S.E. Dutton, Free-spin dominated magnetocaloric effect in dense Gd^{3+} double perovskites, Chem. Mater. 34 (2022) 3440–3450, https://doi.org/10.1021/acs.chemmater.2c00261.

[14] C. Delacotte, T.A. Pomelova, T. Stephant, T. Guizouarn, S. Cordier, N.G. Naumov, P. Lemoine, $NaGdS_2$: a promising sulfide for cryogenic magnetic cooling, Chem. Mater. 34 (2022) 1829–1837, https://doi.org/10.1021/acs.chemmater.1c04105.

[15] P. Mukherjee, S.E. Dutton, Enhanced magnetocaloric effect from Cr substitution in ising lanthanide gallium garnets $Ln_3CrGa_4O_{12}$ (ln = Tb, Dy, Ho), Adv. Funct. Mater. 27 (2017): 1701950, https://doi.org/10.1002/adfm.201701950.

[16] N.K. Chogondahalli Muniraju, R. Baral, Y. Tian, R. Li, N. Poudel, K. Gofryk, N. Barisic, B. Kiefer, J.H. Ross Jr., H.S. Nair, Magnetocaloric effect in a frustrated Gd-Garnet with no long-range magnetic order, Inorg. Chem. 59 (2020) 15144–15153, https://doi.org/10.1021/acs.inorgchem.0c02074.

[17] A.C. Sackville Hamilton, G.I. Lampronti, S.E. Rowley, S.E. Dutton, Enhancement of the magnetocaloric effect driven by changes in the crystal structure of Al-doped GGG, $Gd_3Ga_{5-x}Al_xO12$ ($0<=x<=5$), J. Phys. Condens. Matter 26 (2014): 116001, https://doi.org/10.1088/0953-8984/26/11/116001.

[18] P. Xu, Z. Ma, P. Wang, H. Wang, L. Li, Excellent cryogenic magnetocaloric performances in ferromagnetic Sr_2GdNbO_6 double perovskite compound, Mater. Today Phys. 20 (2021): 100470, https://doi.org/10.1016/j.mtphys.2021.100470.

[19] T. Gruner, J. Chen, D. Jang, J. Banda, C. Geibel, M. Brando, F.M. Grosche, Metallic local-moment magnetocalorics as a route to cryogenic refrigeration, Commun. Mater. 5 (2024) 63, https://doi.org/10.1038/s43246-024-00494-4.

[20] Y. Tokiwa, S. Bachus, K. Kavita, A. Jesche, A.A. Tsirlin, P. Gegenwart, Frustrated magnet for adiabatic demagnetization cooling to milli-Kelvin temperatures, Commun. Mater. 2 (2021) 42, https://doi.org/10.1038/s43246-021-00142-1.

[21] M. Kleinhans, K. Eibensteiner, J.C. Leiner, J. Spallek, A. Regnat, C. Pfleiderer, Magnetocaloric properties of $(RE)_3Ga_5O_{12}$ (RE= Tb, Gd, Nd, Dy), Phys. Rev. Appl. 19 (2023): 014038, https://doi.org/10.1103/PhysRevApplied.19.014038.

[22] B. Wolf, U. Tutsch, S. Dörschug, C. Krellner, F. Ritter, W. Assmus, M. Lang, Magnetic cooling close to a quantum phase transition-the case of $Er_2Ti_2O_7$, J. Appl. Phys. 120 (2016): 142112, https://doi.org/10.1063/1.4961708.

[23] Z.W. Yang, J. Zhang, B. Liu, X. Zhang, D. Lu, H. Zhao, M. Pi, H. Cui, Y.J. Zeng, Z. Pan, Y. Shen, S. Li, Y. Long, Exceptional magnetocaloric responses in a gadolinium silicate with strongly correlated spin disorder for Sub-Kelvin magnetic cooling, Adv. Sci. 11 (2024): 2306842, https://doi.org/10.1002/advs.202306842.

[24] E. Tugova, N. Bobrysheva, A. Selyutin, V. Gusarov, Magnetic properties of complex oxides $Gd_2SrM_2O_7$ (M= Fe, Al), Russ. J. Gen. Chem. 78 (2008) 2000–2001, https://doi.org/10.1134/S1070363208110029.

[25] I. Zvereva, Y.E. Smirnov, J. Choisnet, Cation distribution and interatomic interactions in oxides with heterovalent isomorphism: VIII. 1 A high-temperature Study of the structure of $Gd_2SrAl_2O_7$, Russ. J. Gen. Chem. 74 (2004) 655–658, https://doi.org/10.1023/B:RUGC.0000039072.46257.b6.

[26] Z.W. Yang, J. Zhang, D. Lu, X. Zhang, H. Zhao, H. Cui, Y.-J. Zeng, Y. Long, Strong magnetocaloric coupling in oxyorthosilicate with dense Gd^{3+} spins, Inorg. Chem. 62 (2023) 5282–5291, https://doi.org/10.1021/acs.inorgchem.3c00421.

[27] C. Wellm, J. Zeisner, A. Alfonsov, M.I. Sturza, G. Bastien, S. Gaß, S. Wurmehl, A.U. B. Wolter, B. Büchner, V. Kataev, Magnetic interactions in the tripod kagome antiferromagnet $Mg_2Gd_3Sb_3O_{14}$ probed by static magnetometry and high-field ESR spectroscopy, Phys. Rev. B 102 (2020): 214414, https://doi.org/10.1103/PhysRevB.102.214414.

[28] J.A. Barclay, W.A. Steyert, Magnetic Refrigeration for Space Applications: Report on a Design Study, Los Alamos National Lab.(LANL), Los Alamos, NM (United States), 1980.

[29] R.D. McMichael, J.J. Ritter, R.D. Shull, Enhanced magnetocaloric effect in $Gd_3Ga_{5-x}Fe_xO_{12}$, J. Appl. Phys. 73 (1993) 6946–6948, https://doi.org/10.1063/1.352443.

[30] P. Mukherjee, A.C. Sackville Hamilton, H.F.J. Glass, S.E. Dutton, Sensitivity of magnetic properties to chemical pressure in lanthanide garnets $Ln_3A_2X_3O_{12}$, Ln = Gd, Tb, Dy, Ho, A = Ga, Sc, In, Te, X = Ga, Al, Li, J. Phys. Condens. Matter 29 (2017): 405808, https://doi.org/10.1088/1361-648X/aa810e.

[31] S. Roy, M. Das, P. Mandal, Large low-field magnetic refrigeration in ferromagnetic insulator $EuTi_{0.9}V_{0.1}O_3$, Phys. Rev. Mater. 2 (2018): 064412, https://doi.org/10.1103/PhysRevMaterials.2.064412.

[32] M. Das, S. Roy, P. Mandal, Giant reversible magnetocaloric effect in a multiferroic $GdFeO_3$ single crystal, Phys. Rev. B 96 (2017): 174405, https://doi.org/10.1103/PhysRevB.96.174405.

[33] X. Moya, E. Defay, V. Heine, N.D. Mathur, Too cool to work, Nat. Phys. 11 (2015) 202–205, https://doi.org/10.1038/nphys3271.

[34] V. Franco, A. Conde, Scaling laws for the magnetocaloric effect in second order phase transitions: from physics to applications for the characterization of materials, Int. J. Refrig. 33 (2010) 465–473, https://doi.org/10.1016/j.ijrefrig.2009.12.019.

[35] J.Y. Law, V. Franco, L.M. Moreno-Ramirez, A. Conde, D.Y. Karpenkov, I. Radulov, K.P. Skokov, O. Gutfleisch, A quantitative criterion for determining the order of magnetic phase transitions using the magnetocaloric effect, Nat. Commun. 9 (2018) 2680, https://doi.org/10.1038/s41467-018-05111-w.

[36] T.D. Shen, R.B. Schwarz, J.Y. Coulter, J.D. Thompson, Magnetocaloric effect in bulk amorphous $Pd_{40}Ni_{22.5}Fe_{17.5}P_{20}$ alloy, J. Appl. Phys. 91 (2002) 5240–5245, https://doi.org/10.1063/1.1456957.